CrossMark

J. Fluid Mech. (2017), *vol.* 821, *pp.* 219–247. © Cambridge University Press 2017
doi:10.1017/jfm.2017.241

Unsteady critical liquid sheet flows

M. Girfoglio[1], F. De Rosa[1], G. Coppola[1] and L. de Luca[1,†]

[1]Department of Industrial Engineering, Aerospace Sector, Università di Napoli 'Federico II', Naples, Italy

(Received 15 February 2016; revised 7 April 2017; accepted 10 April 2017; first published online 18 May 2017)

The unsteady global dynamics of a gravitational liquid sheet interacting with a one-sided adjacent air enclosure (commonly referred to as nappe oscillation configuration) is addressed under the assumptions of potential flow and the presence of surface tension effects. From a theoretical viewpoint the problem is challenging, because from previous literature it is known that the equation governing the evolution of small disturbances exhibits a singularity at the vertical station where the local flow velocity equals the capillary wave velocity (local critical condition), although the solution to the problem has not yet been found. The equation governing the local dynamics resembles one featuring the forced vibrations of a string of finite length, formulated in the reference frame moving with the flow velocity, and exhibits both slow and fast characteristic curves. From the global system perspective the nappe behaves as a driven damped spring–mass oscillator, where the inertial effects are linked to the liquid sheet mass and the spring is represented by the equivalent stiffness of the air enclosure acting on the displacement of the compliant nappe centreline. A suited procedure is developed to remove the singularity of the integro-differential operator for Weber numbers less than unity. The investigation is carried out by means of a modal (i.e. time asymptotic) linear approach, which is corroborated by numerical simulations of the governing equation and supported by systematic comparisons with experimental data from the literature, available in the supercritical regime only. As regards the critical regime for the unit Weber number, the major theoretical result is a sharp increase in oscillation frequency as the flow Weber number is gradually reduced from supercritical to subcritical values due to the shift of the prevailing mode from the slow one to the fast one.

Key words: capillary flows, interfacial flows (free surface), waves/free-surface flows

1. Introduction

The basic nature of the global dynamics of gravitational (i.e. spatially developing) liquid sheet flows, in the presence of surface tension effects, depends crucially on the inlet Weber number, $We = \rho_l U_{in}^2 H_{in}/2\sigma$, where ρ_l is the liquid density, U_{in} the inlet liquid velocity, H_{in} the initial thickness of the sheet, σ the air–liquid surface tension. When $We > 1$, the local Weber number, $We_l = U^2/c^2$, with U and $c = \sqrt{2\sigma/(\rho_l H)}$ being the local flow and capillary waves velocity (de Luca & Costa 1997*b*), respectively, is also greater than unity at each streamwise location, so that the flow can be

† Email address for correspondence: deluca@unina.it

https://doi.org/10.1017/jfm.2017.241 Published online by Cambridge University Press

defined as supercritical everywhere. When $We < 1$, an initial region exists where the sheet flow is subcritical, up to the critical location, downstream of which the flow becomes supercritical. In a previous paper about the unsteady dynamics of water bells, Brunet, Clanet & Limat (2004), resorting to an analogy between sound waves and capillary waves, termed the line separating the two regions transonic. From a theoretical viewpoint, the problem under study is not straightforward, because it is known (Finnicum, Weinstein & Rushak 1993; Weinstein *et al.* 1997; Ramos 2001, 2003) that the equation governing the evolution of small disturbances exhibits a singularity just at the critical station and the solution to the problem has not yet been found. All these authors evidence and analyse the nature of the singularity, but no one has definitely solved the time-dependent equations governing the behaviour of the subcritical nappe. Thus, the present work aims at facing the problem to make up for this lack of information.

Although physically the singularity is due to surface tension effects, and therefore it can occur in various situations involving different models of external ambient pressure interacting with the liquid sheet, in this paper we will refer to the so-called nappe oscillation configuration. It is well known that a thin water sheet (curtain or nappe), flowing freely from a top opening, gives rise to low-frequency periodic oscillations when interacting with an air enclosure which acts as a resonator. Such a behaviour, commonly referred to as the nappe oscillation phenomenon (Schwartz 1964), arises from a mutually induced mechanism among the oscillations of the curtain and the pressure fluctuations in the air enclosure adjacent to one side of the sheet, with the other one being in contact with an unperturbed ambient (Naudascher & Rockwell 1994). The flow of waterfalls, naturally outpoured or generated by the overflow of water over long crests of dams or weirs, represents a typical example of such a configuration. The noise produced by the oscillation of the waterfall can be radiated far away from the source and may cause problems such as vibrations in doors or windowpanes in buildings nearby, and even structural damages to the dam itself (Crookston & Tullis 2013). In this paper it will be shown that, around the critical regime, the theory predicts a sharp increase in nappe oscillation frequency as the flow Weber number is gradually reduced, from supercritical to subcritical values.

Theoretically, the physical problem involves a spatially developing fluid flow system which is able to sustain a variety of wave patterns. Although the spatio-temporal evolution of planar free-falling liquid sheet flows has been widely discussed, mainly in the context of linear stability analysis (Lin, Lian & Creighton 1990; de Luca & Costa 1997*a*; de Luca 1999; Barlow, Helenbrook & Lin 2011), little attention has been paid to modelling the global coupling between advection and reaction effects (where the term global refers to the system as a whole) when the curtain interacts with a closed air chamber. Binnie (1974) carried out the first relevant study addressing the nappe oscillation phenomenon from both theoretical and experimental points of view. In particular, he formulated a linearized physical model governing the spatio-temporal evolution of disturbances where surface tension effects were neglected. The flow patterns emerging in his experiments, limited to supercritical regimes, were related to the single modes of the eigenvalues spectrum. Binnie (1974) suggested that the actual frequency selection mechanism could depend on interfacial viscous shear, due to the ambient air and ignored in the theory. Among more recent experimental contributions noticeable are the works of Sato *et al.* (2007), and Mori *et al.* (2012), who found a strong correlation between the oscillation frequency of the water sheet and the pressure fluctuation in the adjacent air chamber. They also carried out a theoretical analysis to examine the modal stability of the sheet vibration by means of

https://doi.org/10.1017/jfm.2017.241 Published online by Cambridge University Press

a complex eigenvalue problem, and compared the less stable mode frequency with the characteristic frequency of a one-degree-of-freedom spring–mass system, with the air into the enclosure being considered as a spring and the water sheet being modelled as a mass. However, the characteristic frequency of the most unstable mode is from 10- to 20 times larger than the frequency experimentally observed in visualizing the nappe oscillation in supercritical conditions. Even the shape of the associate eigenfunction is completely different than that monitored in experiments.

Le Grand *et al.* (2006) reported theoretical as well as experimental findings on the characteristics of the global dynamics of liquid sheets, but their work is concerned with a different context, i.e. the case of symmetrical semi-infinite boundary air environments.

Within the framework of the linear non-modal stability theory Schmid & Henningson (2002) found time-periodic oscillations in the optimal amplification of the disturbances energy, and correlated the period of such oscillations to the quasi-constant spacing among the imaginary parts of eigenvalues. They concluded that the phenomenon under study is governed not by a single mode, but by the (linear) interaction of many modes. Such a global feature of the spectrum, obtained neglecting the surface tension, closely agrees with the low-frequency oscillations typically observed in real systems, as confirmed also by Coppola & de Luca (2006) who considered a general toy model.

The global dynamics of nappe oscillation has been recently revisited by De Rosa, Girfoglio & de Luca (2014), who extended the analysis of Schmid & Henningson (2002), and found a strong analogy to the edge-tones problem, i.e. acoustic tones produced when a jet of air strikes a wedge-shaped edge; a simple relationship determining the dimensionless resonance frequencies was also reported. Following De Rosa *et al.* (2014), in the present paper the flow is assumed inviscid and the problem is arranged in a one-dimensional formulation along the streamwise direction. The interaction with the external environment refers to an air enclosure located on one side of the sheet. Physical insights on sheet centreline sinuous modes will show that the nappe dynamics features the propagation of two wave fronts both directed downstream or one downstream and the other one upstream, depending on whether the flow is supercritical or subcritical, respectively. In every situation the inlet section is considered as a perfectly reflecting boundary. As regards an additional boundary condition, in the former regime it prescribes a null centreline slope at the inlet; in the latter it is imposed just at the singularity station, by enforcing the boundedness requirement of the centreline slope there. An additional analytical investigation on the nature of the singularity, based on the Frobenius theory, predicts that the flow is unconditionally stable for any $We < 1$ and that the temporal growth rate of disturbances is bounded.

The findings of the spectral analysis confirm the theoretical predictions anticipated above. They closely agree with numerical simulations of the partial differential equation governing the global evolution of the disturbances in the space–time domain, starting from an initial Gaussian-like shape. Data also agree quantitatively with previous experimental findings of the literature at relatively high Weber numbers (supercritical regime).

The paper is organized as follows: the physical model is developed in § 2, with the overall insights on the nappe dynamics being reported in § 3. The linear stability analysis, including the description of the procedure employed to remove the singularity of the operator, is illustrated in § 4. The overall results are presented in § 5 and major conclusions are drawn up in § 6.

https://doi.org/10.1017/jfm.2017.241 Published online by Cambridge University Press

2. Physical modelling

To derive a physical model of the unsteady evolution of an inviscid gravitational liquid sheet, the assumptions of thin curtain and plug flow are adopted (Mehring & Sirignano 1999; Coppola, De Rosa & de Luca 2013; De Rosa *et al.* 2014). It has to be stressed in particular that, contrary to the recent paper of De Rosa *et al.* (2014), the surface tension effect is fully included since, as will be discussed later on, the presence of the singularity at the critical line depends crucially on the surface tension.

Although in principle singularities arise also in aerated or open configurations (Finnicum *et al.* 1993; Weinstein *et al.* 1997; Ramos 2001, 2003; Brunet *et al.* 2004), here we consider the boundary pressure field within a two-dimensional air enclosure delimited by the sheet itself, rigid walls and a lower basin; namely, we will address the unsteady behaviour of the configuration generally referred to as nappe oscillation. Splashing effects are neglected. Furthermore, the investigation will be restricted to the occurrence of one-dimensional surface wave patterns. One can expect that oblique waves (i.e. developing along the spanwise direction) occur when extending the study to three-dimensional configurations, as already found experimentally by Le Grand *et al.* (2006) in the case of symmetrical semi-infinite boundary air environments.

Figure 1 shows the schematic of the geometrical configuration under consideration. In the unperturbed condition the liquid flows along the vertical x-direction with a steady velocity and two symmetrical free interfaces. The definitions of the unsteady centreline location ℓ and thickness h of the sheet are given, in terms of the interface positions $y^{\pm}$, as follows

$$\ell^{\star}(x^{\star}, t^{\star}) = \frac{y^{\star+}(x^{\star}, t^{\star}) + y^{\star-}(x^{\star}, t^{\star})}{2} \tag{2.1}$$

$$h^{\star}(x^{\star}, t^{\star}) = y^{\star+}(x^{\star}, t^{\star}) - y^{\star-}(x^{\star}, t^{\star}), \tag{2.2}$$

where superscripts $\pm$ refer to right and left interfaces, respectively, and t^* is the time. Here as elsewhere the star denotes dimensional quantities. Note that the inlet velocity and sheet thickness of the basic flow employed in the Introduction to define the Weber number were denoted without a star apex, for the sake of simplicity; the star is omitted similarly in figure 1. Furthermore, the general definition $\varphi^{\star\pm}(x^{\star}, t^{\star}) = \varphi^{\star}(x^{\star}, y^{\star\pm}, t^{\star})$ will be adopted in the following, φ being any of the flow variables u, v or p (where u and v are the streamwise and lateral liquid velocity components, respectively, and p is liquid pressure).

2.1. *Governing equations*

The starting mathematical framework is given by the two-dimensional Euler equations in which gravity is retained, closed by the kinematic and dynamic conditions imposed at the free interfaces.

The assumption of a thin sheet with respect to the wavelength of a disturbance allows one to consider local plug-type velocity profiles for u and v across the nappe thickness. To derive the governing equations the following procedure can be adopted: the mass and x-momentum balances are formulated over a generic slice of the curtain of length dx; the y-momentum equation is integrated along the lateral coordinate y; the unsteady quantities are considered as the sum of a steady contribution and a perturbation (or fluctuation)

$$u^* = U^* + u'^* \tag{2.3}$$

$$v^* = V^* + v'^* \tag{2.4}$$

https://doi.org/10.1017/jfm.2017.241 Published online by Cambridge University Press

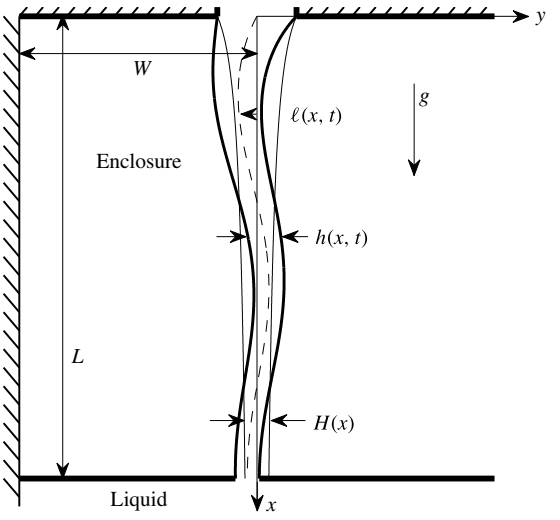


FIGURE 1. Sketch of the model configuration.

$$p^* = P^* + p'^* \tag{2.5}$$

$$h^* = H^* + h'^* \tag{2.6}$$

$$y^{*\pm} = Y^{*\pm} + y'^{*\pm}, \tag{2.7}$$

where capital letters (here as elsewhere) denote basic (steady) quantities and prime the corresponding perturbations. Under the assumption of small perturbations, and $V^* = 0$, the linearized forms of continuity, x-momentum and y-momentum equations are written, respectively:

$$\frac{\partial h'^\star}{\partial t^\star} + \frac{\partial}{\partial x^\star}\left(U^\star h'^\star + H^\star u'^\star\right) = 0 \tag{2.8}$$

$$\frac{\partial u'^\star}{\partial t^\star} + \frac{\partial}{\partial x^\star}\left(U^\star u'^\star\right) = -\frac{1}{\rho_l}\frac{\partial p'^\star}{\partial x^\star} \tag{2.9}$$

$$\frac{\partial v'^\star}{\partial t^\star} + U^\star \frac{\partial v'^\star}{\partial x^\star} = -\frac{1}{\rho_l H^\star}(p'^{\star +} - p'^{\star -}), \tag{2.10}$$

where ρ_l is the liquid density.

The interface kinematic and pressure jump boundary conditions are, respectively:

$$v^{\star\pm} = \frac{\partial y^{\star\pm}}{\partial t^\star} + u^{\star\pm}\frac{\partial y^{\star\pm}}{\partial x^\star} \tag{2.11}$$

$$p^{\star\pm} = p_a^{\star\pm} \mp \sigma \frac{\partial^2 y^{\star\pm}}{\partial x^{\star 2}}\left[1 + \left(\frac{\partial y^{\star\pm}}{\partial x^\star}\right)^2\right]^{-3/2}, \tag{2.12}$$

where $p_a^{\star\pm}(x^\star, t^\star)$ is the local value of the external ambient pressure and σ is the surface tension coefficient.

The difference between the fluctuating boundary pressures of (2.10) can be expressed in terms of perturbations of ambient pressure and interface locations

https://doi.org/10.1017/jfm.2017.241 Published online by Cambridge University Press

by linearizing in perturbation quantities the dynamic boundary condition (2.12):

$$p'^{\star\pm} = p_a'^{\star\pm} \mp \sigma \left[1 + \left(\frac{\mathrm{d}Y^{\star\pm}}{\mathrm{d}x^\star}\right)^2\right]^{-3/2} \cdot \left\{ \frac{\partial^2 y'^{\star\pm}}{\partial x^{\star 2}} - 3 \frac{\dfrac{\mathrm{d}^2 Y^{\star\pm}}{\mathrm{d}x^{\star 2}} \dfrac{\mathrm{d}Y^{\star\pm}}{\mathrm{d}x^\star} \dfrac{\partial y'^{\star\pm}}{\partial x^\star}}{1 + \left(\dfrac{\mathrm{d}Y^{\star\pm}}{\mathrm{d}x^\star}\right)^2} \right\}. \tag{2.13}$$

The result is then recast in the form:

$$p'^{\star+} - p'^{\star-} = \widetilde{p}_a'^{\star} - 2\sigma \frac{\partial}{\partial x^\star}\left[F^\star \frac{\partial \ell'^\star}{\partial x^\star}\right], \tag{2.14}$$

with $F^\star = [1 + (\mathrm{d}H^\star/\mathrm{d}x^\star)^2/4]^{-3/2}$, and $\widetilde{p}_a^\star = p_a^{\star+} - p_a^{\star-}$. Note also that $|Y^{*\pm}| = H^*/2$.

Equation (2.10) has to be coupled with the linearized kinematic boundary condition, which can be properly expressed in terms of the centreline deflection only:

$$v'^\star = \frac{\partial \ell'^\star}{\partial t^\star} + U^\star \frac{\partial \ell'^\star}{\partial x^\star}. \tag{2.15}$$

Equations (2.10) and (2.15) constitute a closed system for the unknown lateral velocity and centreline perturbations, representing the so called antisymmetric sinuous solution to the unsteady perturbed field.

It is easily observed that (2.8) and (2.9) represent, on the other hand, the symmetric, or varicose, or even squeezing solution for the perturbed longitudinal velocity and sheet thickness. In fact, the liquid pressure (which is constant in this symmetric case, i.e. $p'^\star = p'^{\star+} = p'^{\star-}$) can be eliminated by taking the half-sum of the right-hand side of (2.13) so as to obtain

$$p'^\star = \overline{p}_a'^\star - \frac{\sigma}{2}\frac{\partial}{\partial x^\star}\left[F^\star \frac{\partial h'^\star}{\partial x^\star}\right], \tag{2.16}$$

where

$$\overline{p}_a^\star = \frac{p_a^{\star+} + p_a^{\star-}}{2}. \tag{2.17}$$

To close the two systems of coupled equations (2.8)–(2.9) and (2.10)–(2.15), expressions for the ambient gas pressure terms $\overline{p}_a'^\star$ and $\widetilde{p}_a'^\star$ as functions of the perturbations of the sheet are required.

The infinitesimal variation of the enclosure volume, resulting from the sheet fluctuation, is given by

$$\mathcal{V}_a'^\star = \int_0^{L^\star} \ell'^\star(x^\star)\,\mathrm{d}x^\star - \frac{1}{2}\int_0^{L^\star} h'^\star(x^\star)\,\mathrm{d}x^\star. \tag{2.18}$$

If we hypothesize that the air within the enclosure encompasses compression/expansion isentropic thermodynamic transformations, we are able to give explicit expressions for the external pressure terms of (2.14) and (2.16), for the two different oscillating modes of the sheet, respectively, as follows:

$$\widetilde{p}_a'^\star = \gamma \frac{P_a^\star}{\mathcal{V}_a^\star}\int_0^{L^\star} \ell'^\star(x^\star)\,\mathrm{d}x^\star \tag{2.19}$$

$$\overline{p}_a'^\star = \frac{\gamma}{4}\frac{P_a^\star}{\mathcal{V}_a^\star}\int_0^{L^\star} h'^\star(x^\star)\,\mathrm{d}x^\star, \tag{2.20}$$

https://doi.org/10.1017/jfm.2017.241 Published online by Cambridge University Press

where γ is the specific heat ratio, $P_a^\star$ is the unperturbed gas pressure into the enclosure and $\mathcal{V}_a^\star = L^\star W^\star - \int_0^{L^\star} H^\star(x^\star)\,\mathrm{d}x^\star/2$ is the corresponding volume in the configuration shown in figure 1.

Substituting the above relationships of the pressure difference and of the average pressure into the streamwise and lateral momentum equations (2.9) and (2.10), respectively, eventually yields:

$$\frac{\partial u'^\star}{\partial t^\star} + \frac{\partial}{\partial x^\star}\left(U^\star u'^\star\right) = \frac{\sigma}{2\rho_l}\frac{\partial^2}{\partial x^{\star 2}}\left[F^\star \frac{\partial h'^\star}{\partial x^\star}\right] \tag{2.21}$$

$$\frac{\partial v'^\star}{\partial t^\star} + U^\star \frac{\partial v'^\star}{\partial x^\star} = \frac{2\sigma}{\rho_l H^\star}\frac{\partial}{\partial x^\star}\left[F^\star \frac{\partial \ell'^\star}{\partial x^\star}\right] - \frac{\gamma}{\rho_l H^\star}\frac{P_a^\star}{\mathcal{V}_a^\star}\int_0^{L^\star} \ell'^\star(x^\star)\,\mathrm{d}x^\star. \tag{2.22}$$

It is worth noting that in deriving (2.21) it is implicitly assumed that the pressure fluctuation inside the air enclosure does not vary in space, according to the model of lumped reaction of the cushion, which is the equivalent of neglecting acoustic modes propagating in the air enclosure. The cushion lumped model is valid if the ratio of the traversing time, $t_a^\star$, of an acoustic perturbation over a typical dimension of enclosure (say $W^\star$), to the oscillation period $T^\star$, is sufficiently small. As will be seen later in discussing experimental comparisons, for typical experimental arrangements this assumption is valid up to frequencies of the order of 100 Hz. The set of two systems of coupled equations (2.8)–(2.21) and (2.15)–(2.22), can be also arrived at by using the theory and the methods of perturbations (De Rosa 2013).

2.2. *Non-dimensional equations and slender sheet approximation*

The governing equations can be conveniently made dimensionless by employing the reference quantities

$$L_r^\star = L^\star, \quad \ell_r^\star = H_{in}^\star, \tag{2.23a,b}$$

$$u_r^\star = U_{in}^\star, \quad v_r^\star = \varepsilon U_{in}^\star, \tag{2.24a,b}$$

$$t_r^\star = L^\star/U_{in}^\star, \quad p_r^\star = \rho_l U_{in}^{\star 2}, \tag{2.25a,b}$$

with $\varepsilon = \ell_r^\star/L_r^\star$ denoting the slenderness parameter (tiny according to the assumptions made in deriving the model). The non-dimensional form has the following results

$$\frac{\partial \ell}{\partial t} + U\frac{\partial \ell}{\partial x} = v \tag{2.26}$$

$$\frac{\partial v}{\partial t} + U\frac{\partial v}{\partial x} = \frac{1}{WeH}\frac{\partial}{\partial x}\left[F\frac{\partial \ell}{\partial x}\right] - \frac{\gamma}{H}\frac{P_a}{\varepsilon\left(\dfrac{W^\star}{L^\star} - \dfrac{\varepsilon}{2}\displaystyle\int_0^1 H\,\mathrm{d}x\right)}\int_0^1 \ell(x)\,\mathrm{d}x \tag{2.27}$$

$$\frac{\partial h}{\partial t} + \frac{\partial}{\partial x}(Uh + Hu) = 0 \tag{2.28}$$

$$\frac{\partial u}{\partial t} + \frac{\partial}{\partial x}(Uu) = \frac{\varepsilon^2}{4We}\frac{\partial^2}{\partial x^2}\left[F\frac{\partial h}{\partial x}\right], \tag{2.29}$$

https://doi.org/10.1017/jfm.2017.241 Published online by Cambridge University Press

where

$$We = \rho_l U_{in}^{\star 2} H_{in}^{\star}/2\sigma \tag{2.30}$$

is the Weber number, already defined in the Introduction, with the exception of the use of the star apex, and $F = [1 + \varepsilon^2/4(\mathrm{d}H/\mathrm{d}x)^2]^{-3/2}$. Note that (2.26)–(2.27) describe the sinuous modes, whilst (2.28)–(2.29) describe the varicose ones.

As extensively discussed in Coppola *et al.* (2013), in the absence of viscosity, an analytical solution for sheet thickness and streamwise liquid velocity of the steady (base) flow can be obtained by performing a parameter-type expansion in the small ratio ε^2 of the unperturbed governing equations. At the zeroth-order expansion, the following non-dimensional Torricelli's free-fall solution for the base flow results:

$$UH = 1 \quad \text{and} \quad U = \sqrt{1 + \frac{2}{Fr}x}, \tag{2.31a,b}$$

where

$$Fr = U_{in}^{\star 2}/gL^{\star} \tag{2.32}$$

denotes the Froude number.

Accordingly, the corresponding lowest-order expansion to (2.26)–(2.29) leads to the slender sheet approximation: for the sinuous mode

$$\frac{\partial \ell}{\partial t} + U\frac{\partial \ell}{\partial x} = v \tag{2.33}$$

$$\frac{\partial v}{\partial t} + U\frac{\partial v}{\partial x} = \frac{1}{WeH}\frac{\partial^2 \ell}{\partial x^2} - \frac{\mathcal{K}}{H}\bar{\ell} \tag{2.34}$$

and for the varicose mode

$$\frac{\partial h}{\partial t} + \frac{\partial}{\partial x}(Uh + Hu) = 0 \tag{2.35}$$

$$\frac{\partial u}{\partial t} + \frac{\partial}{\partial x}(Uu) = 0, \tag{2.36}$$

with

$$\mathcal{K} = \gamma \frac{P_a}{\varepsilon}\frac{L^{\star}}{W^{\star}} \tag{2.37}$$

and

$$\bar{\ell} = \int_0^1 \ell \, \mathrm{d}x \tag{2.38}$$

denoting the average sinuous deflection of the sheet.

To sum up, three independent dimensionless parameters for the problem under study are considered: the Weber number We, the Froude number Fr and the equivalent air stiffness $\mathcal{K}$. Note explicitly that in the present analysis the air stiffness includes simultaneously the effects of the undisturbed pressure within the enclosure, of the enclosure width and of the slenderness ratio $\varepsilon = H_{in}^{\star}/L^{\star}$, which in principle have

https://doi.org/10.1017/jfm.2017.241 Published online by Cambridge University Press

to be taken into account separately. More importantly, one should note that, for practical physical cases of water sheet surrounded by air, ρ_l, σ, γ and $P_a^\star$ have to be considered as fixed quantities, and it is easy to verify that given values of the dimensionless quantities We, Fr, $\mathcal{K}$ and ε determine a unique set of values $U_{in}^\star$, $H_{in}^\star$, $L^\star$ and $W^\star$, and *vice versa*.

Note also that (2.35)–(2.36) governing the evolution of the varicose modes are not able to sustain any oscillating wave pattern in the configuration here adopted, reducing to simple advection equations. Therefore, the study will be focused hereinafter on the sinuous disturbances only, equations (2.33)–(2.34). Particular attention has to be paid to enforce the boundary conditions depending on whether the inlet Weber number is supercritical or subcritical. In fact, in the first case two boundary conditions are prescribed at the inlet location, $x = 0$, namely $\ell(0) = 0$ and $\partial\ell/\partial x(0) = 0$ (which in turn means $v(0) = 0$), whilst in the latter case the condition, $\ell(0) = 0$, is retained at the inlet section, and another one has to be considered at a downstream location. We will discuss that the second condition is employed to remove the singularity of the equation and is enforced at just the singularity location.

3. Overall insight into the nappe dynamics

Let us start to reconsider the system of equations (2.33)–(2.34) in terms of a single second-order integro-differential equation

$$\frac{\partial^2\ell}{\partial t^2} + 2U\frac{\partial^2\ell}{\partial x\partial t} + U\left(U - \frac{1}{We}\right)\frac{\partial^2\ell}{\partial x^2} + U\frac{\partial U}{\partial x}\frac{\partial\ell}{\partial x} = -\mathcal{K}U\bar{\ell}. \tag{3.1}$$

According to the basic theory of the second-order linear partial differential equations, the equation has a hyperbolic nature (Howison 2005, p. 96) for any $x \geqslant 0$, with the discriminant of its principal part, namely U/We, being always positive. Thus, the equation features two real and distinct characteristics on the entire physical domain.

In terms of substantial derivative the above equation can be conveniently rewritten as

$$\frac{\mathrm{D}^2\ell}{\mathrm{D}t^2} - \frac{U}{We}\frac{\partial^2\ell}{\partial x^2} = -\frac{\mathcal{K}}{H}\bar{\ell}, \tag{3.2}$$

which is analogous to the classic one featuring forced transverse vibrations of a finite length string (Kinsler *et al.* 2000). The role played by the air stiffness $\mathcal{K} \geqslant 0$ is crucial in characterizing the dynamics of the self-induced wave patterns evolving into the nappe. If $\mathcal{K} = 0$ the equation is trivial, reducing it to the simple wave equation with velocity $\pm\sqrt{U/We}$ relative to that of the basic flow U, and is basically equipped with a perfectly reflecting boundary condition at the inlet, $\ell(0) = 0$, and free-outflow condition at the outlet. In the fixed reference frame the wave velocity is

$$U \pm \sqrt{\frac{U}{We}}, \tag{3.3}$$

which can also be recast in the form

$$U\left(1 \pm \sqrt{\frac{1}{We_l}}\right). \tag{3.4}$$

https://doi.org/10.1017/jfm.2017.241 Published online by Cambridge University Press

It can be easily verified that in the absence of enclosure reaction (i.e. in the case of no forcing) and for constant U velocity, the wave-like equation (3.1) admits solutions of the kind

$$\ell = A\mathrm{e}^{\mathrm{i}k(x-at)}, \tag{3.5}$$

where $a = U(1 \pm \sqrt{1/We_l})$, k is any real wavenumber and A is a constant. We will see that even in cases where U is not a constant, the equation is verified for a proper average wave velocity $\bar{a}$.

Therefore one expects that any compact support disturbance introduced in the field splits up in two parts: in subcritical conditions the one travelling in the upstream direction, after reflection at the inlet boundary, is eventually expelled through the lower boundary as the other one, initially travelling in the downstream direction, does too; in the supercritical regime both perturbations produced by the initial splitting travel towards the outlet and are expelled. If no input is introduced at the upper boundary, after a finite time any solution vanishes, with the disturbance being expelled. Conversely, the presence of the forcing modifies this scenario in such a way that the temporal evolution of the disturbance is by no means identically null after a finite time. As pointed out by previous numerical contributions (Schmid & Henningson 2002; De Rosa *et al.* 2014), the theory (Kinsler *et al.* 2000) predicts that the term forcing the sheet transverse vibrations, namely the air chamber reaction, generates separate resonance modes so that the corresponding eigenvalues of the spectrum have different real coefficients (and almost evenly spaced imaginary coefficients, with the distance between them corresponding to the crossing time over the sheet length and characterizing the low-frequency oscillations).

Due to the perfect reflecting character of the inlet boundary, any disturbance propagating towards the upstream direction is only reflected and its asymptotic behaviour will be the same as that of the disturbances propagating on the downstream direction. As a consequence, two branches of spectra in supercritical cases and just one branch in subcritical cases are predicted. Hence, in the critical regime, when passing from subcritical to supercritical conditions, the appearance of another branch of the spectrum, associated with the slower characteristic curve, is expected, whilst the faster branch should be continuous.

Such predictions will be confirmed by the subsequent spectral analysis, which is further corroborated by numerical simulations.

In order to have a global system perspective, the equations can be rearranged by introducing integral quantities depending on the sheet extension as a whole. After expressing the substantial derivative in explicit form, integrating (3.2) over the length of the sheet yields:

$$\bar{H}\frac{\mathrm{d}^2\bar{\ell}}{\mathrm{d}t^2} + 2\frac{\mathrm{d}\bar{\ell}}{\mathrm{d}t} + \mathcal{K}\bar{\ell} = \underbrace{-2\frac{\mathrm{d}}{\mathrm{d}t}\int_0^1 x\frac{\partial \ell}{\partial x}\,\mathrm{d}x - \left[U\left(1 - \frac{1}{WeU}\right)\cdot\frac{\partial \ell}{\partial x}\right]_0^1}_{f_i}, \tag{3.6}$$

where f_i represents the self-induced forcing acting on an elastic oscillator of stiffness $\mathcal{K}$. According to the development of De Rosa *et al.* (2014), the following position has been made:

$$\bar{H} = \int_0^1 H\,\mathrm{d}x \tag{3.7}$$

https://doi.org/10.1017/jfm.2017.241 Published online by Cambridge University Press

and the boundary condition at the inlet location, $\ell(0) = 0$, has been considered. Quantities at the inlet and outlet boundaries are denoted with the subscripts 0 and 1, respectively. This notation will be used hereafter for all the boundary quantities. Equation (3.6) exhibits a strict analogy with the motion equation of an elastic oscillator, where $\bar{H}$ denotes the mass of the liquid sheet and $\mathcal{K}$ is the equivalent spring stiffness of the enclosure air. A proper manipulation led to extracting a damping term. In the supercritical regime the condition $\partial\ell/\partial x|_0 = 0$ is enforced. At large times one can expect the emergence of a characteristic mode which corresponds to the global response of the system behaving as a forced–damped oscillator. Of course, since the oscillator works in driven regime, the oscillation period does not corresponds to the natural frequency of oscillation and, in general, it cannot be determined in analytical closed form.

To sum up the nappe dynamics consists in the mutual interaction of the centreline local deflection with the compliant air chamber which behaves as a spring acting on the average sheet deflection. Equation (3.2) shows that the local deflection is forced by the global reaction of the spring, whilst the dynamics of the global spring–mass oscillator is driven by a combination of local displacement values, as described by (3.6). This interpretation has been carefully verified by De Rosa *et al.* (2014) who monitored frequency and phase of the forcing term f_i in connection with spring–mass natural frequency and its phase lag. Self-forced spring–mass behaviour was experimentally found by Binnie (1974), Sato *et al.* (2007), as well as Brunet *et al.* (2004) in the context of oscillating water bells.

4. Linear stability analysis

A comprehensive methodology to analyse the asymptotic global behaviour of the nappe dynamics lies in formulating a boundary value eigenvalues problem. This can be conveniently carried out starting from (2.33)–(2.34) and enforcing the global temporal modes position, i.e. assuming the following form of the disturbances: $\ell(x, t) = \hat{\ell}(x) \cdot \mathrm{e}^{\lambda t}$ and $v(x, t) = \hat{v}(x) \cdot \mathrm{e}^{\lambda t}$, where $\hat{\ell}$ and $\hat{v}$ are eigenfunctions and λ is the complex eigenvalue. This allows the governing equations to be recast into the following matrix form

$$\lambda \begin{pmatrix} \hat{\ell} \\ \hat{v} \end{pmatrix} = \mathcal{A} \begin{pmatrix} \hat{\ell} \\ \hat{v} \end{pmatrix}, \tag{4.1}$$

where the spatial operator is

$$\mathcal{A} \equiv \begin{pmatrix} -U \cdot \mathcal{D} & -\mathcal{I} \\ \dfrac{U}{We} \cdot \mathcal{D}^2 - \dfrac{\mathcal{K}}{H} \displaystyle\int_0^1 \mathrm{d}x & -U \cdot \mathcal{D} \end{pmatrix}, \tag{4.2}$$

with $\mathcal{I}$ denoting the identity operator, and $\mathcal{D}$ and $\mathcal{D}^2$ the first and the second spatial derivatives, respectively.

Eigenvalues and eigenfunctions are numerically computed by means of a Chebyshev collocation method in MATLAB environment, where both differential and integral terms are spectrally accurate.

As has already been anticipated, for inlet supercritical conditions, $We > 1$, the two boundary conditions are both imposed at the inlet section, i.e.

$$\hat{\ell}(0) = 0 \tag{4.3}$$

$$\left.\frac{\partial \hat{\ell}}{\partial x}\right|_0 = 0. \tag{4.4}$$

https://doi.org/10.1017/jfm.2017.241 Published online by Cambridge University Press

On the contrary, for the subcritical inlet, $We < 1$, due to the upstream directed wave characteristic velocity $U - \sqrt{U/We}$, the perfectly reflecting conditions $\hat{\ell}(0) = 0$ can only be retained at the inlet boundary. On the other hand, the eigenvalues equation becomes singular and the condition really removing this singularity constitutes the required second boundary condition.

4.1. *Singularity treatment*

Enforcing the temporal modes position on (3.1) leads to the following equation

$$\frac{\mathrm{d}}{\mathrm{d}x}\left[\left(U - \frac{1}{We}\right)\frac{\mathrm{d}\hat{\ell}}{\mathrm{d}x}\right] + 2\lambda\frac{\mathrm{d}\hat{\ell}}{\mathrm{d}x} + \lambda^2\frac{1}{U}\hat{\ell} = -\mathcal{K}\bar{\hat{\ell}}. \tag{4.5}$$

This is a Sturm–Liouville-like eigenvalue integro-differential equation. It is singular since the second-order term coefficient vanishes at the location where the flow, accelerating due to gravity, reaches a critical velocity equal to $1/We$. This singularity has been removed by developing the following procedure.

Integrating (4.5) from the inlet location to the generic location x and resolving for $\partial\hat{\ell}/\partial x$ (by taking into account the kinematic boundary condition), yield an expression for the local slope of the sheet centreline, which depends on the slope value at the inlet location

$$\frac{\partial\hat{\ell}}{\partial x} = \frac{-\mathcal{K}x\bar{\hat{\ell}} - \lambda\hat{\ell} - \lambda\displaystyle\int_0^x \frac{\hat{v}}{U}\,\mathrm{d}\xi + \left(1 - \frac{1}{We}\right)\left.\frac{\partial\hat{\ell}}{\partial x}\right|_0}{U - \dfrac{1}{We}}. \tag{4.6}$$

It has already been stated that in supercritical conditions, since the perturbations do not travel upstream, it is generally assumed $\partial\hat{\ell}/\partial x|_0 = 0$, as observed also experimentally by Finnicum *et al.* (1993) in the steady state situation. On the other hands, note that in a supercritical regime the denominator never vanishes in any location. The scenario changes dramatically in subcritical regime since at the critical station where the local Weber number is unity, the denominator of (4.6) vanishes. Since for inlet Weber numbers weakly less than unity the sheet can survive without rupture, one can hypothesize that the sheet assumes an initial slope which is able to eliminate this singularity (Finnicum *et al.* 1993). The idea is to evaluate the initial slope $\partial\hat{\ell}/\partial x|_0$ which nullifies the numerator of (4.6) and to substitute it into the equation itself, so as to obtain an undetermined ratio. We find

$$\left.\frac{\partial\hat{\ell}}{\partial x}\right|_0 = \frac{\mathcal{K}x_s\bar{\hat{\ell}} + \lambda\hat{\ell}(x_s) + \lambda\displaystyle\int_0^{x_s}\frac{\hat{v}}{U}\,\mathrm{d}\xi}{1 - \dfrac{1}{We}} \tag{4.7}$$

and the relationship of the slope at any generic station x assumes the form

$$\frac{\partial\hat{\ell}}{\partial x} = \frac{\mathcal{K}(x_s - x)\bar{\hat{\ell}} + \lambda\hat{\ell}(x_s) - \lambda\hat{\ell}(x) - \lambda\displaystyle\int_{x_s}^x \frac{\hat{v}}{U}\,\mathrm{d}\xi}{U - \dfrac{1}{We}}, \tag{4.8}$$

https://doi.org/10.1017/jfm.2017.241 Published online by Cambridge University Press

where x_s is the location where $U = 1/We$, namely where $We_l = 1$, given by

$$x_s = \frac{Fr(1 - We^2)}{2We^2}. \tag{4.9}$$

Applying de L'Hôpital's rule allows us to calculate the singular limit as

$$\left.\frac{\partial \hat{\ell}}{\partial x}\right|_{x_s} = \frac{-\mathcal{K}\bar{\hat{\ell}} - \lambda We \cdot \hat{v}(x_s)}{\lambda + We/Fr}. \tag{4.10}$$

In conclusion, for subcritical inlet, the boundary conditions to be enforced in solving the eigenvalue problem are expressed by (4.10) together with $\hat{\ell}(0) = 0$.

An analytical study of the singularity has been developed in order to provide further insights on the modal behaviour of the system. We will limit ourselves to stressing just some theoretical considerations which are useful in confirming theoretical results although, as will be seen, a complete analytical solution can be obtained, at least for certain values of the dimensionless parameters *We* and *Fr*. For our purposes, we neglect the pressure term in (4.5), the presence of which does not influence the singularity features, and we refer to the following equation (the first derivative which appears in (4.5) has been developed)

$$\underbrace{U^2\left(1 - \frac{1}{We_l}\right)}_{P}\frac{\mathrm{d}^2\hat{\ell}}{\mathrm{d}x^2} + \underbrace{(2U\lambda + 1)}_{Q}\frac{\mathrm{d}\hat{\ell}}{\mathrm{d}x} + \underbrace{\lambda^2}_{R}\hat{\ell} = 0. \tag{4.11}$$

It is easily verified that the following conditions are satisfied:

$$P(x_s) = 0 \tag{4.12}$$

$$\lim_{x\to x_s}(x - x_s)\frac{Q}{P} = \frac{Fr}{We}(2\lambda + We) \quad \text{(finite)} \tag{4.13}$$

$$\lim_{x\to x_s}(x - x_s)^2\frac{R}{P} = 0 \quad \text{(finite)}. \tag{4.14}$$

Therefore, the singular abscissa can be classified as a regular singular point (Boyce & DiPrima 2008). According to the basic Frobenius theory (Bender & Orszag 1999), the solution to (4.11) around the singularity location can be expressed by means of the following series expansion:

$$\hat{\ell}(x, s) = (x - x_s)^\alpha \sum_{n=0}^{\infty} a_n (x - x_s)^n. \tag{4.15}$$

Substituting the above position in (4.11) and imposing the equality of same-order terms lead us to (for $n = 0$) the following indicial equation

$$a_0\left[\frac{1}{We}\alpha(\alpha - 1) + \left(\frac{1}{We} + \frac{2}{We^2}\lambda\right)\alpha\right] = 0. \tag{4.16}$$

Since by definition $a_0 \neq 0$, equation (4.16) yields

$$\alpha_1 = 0 \quad \alpha_2 = -\frac{2Fr\lambda}{We}. \tag{4.17a,b}$$

https://doi.org/10.1017/jfm.2017.241 Published online by Cambridge University Press

The structure of the solution depends mainly on the value assumed for the difference of the roots $\alpha_1 - \alpha_2$ (particular cases occur when α_1 and α_2 are equal, or differ by an integer, and the singular equation has a second solution involving a logarithmic term). In the present analysis, this characteristic difference is given by

$$\alpha_1 - \alpha_2 = \frac{2Fr\lambda}{We}. \tag{4.18}$$

Therefore, the particular cases can be excluded and the solution to the singular differential equation is given by the linear combination of two Frobenius series

$$\hat{\ell}(x, s) = C_1 \sum_{n=0}^{\infty} a_{n,1}(x - x_s)^n + C_2(x - x_s)^{-(2\lambda Fr/We)} \sum_{n=0}^{\infty} a_{n,2}(x - x_s)^n, \tag{4.19}$$

where C_1 and C_2 are constants to be determined by taking into account the boundary conditions. Note that, being $\alpha_1 = 0$, the first Frobenius series reduces to a standard power series expansion (Taylor series).

It is worthwhile analysing the convergence properties of the series expansion (4.19). Equation (4.11) shows another regular singular point at $U = 0$ ($\bar{x} = -Fr/2$). The radius of convergence of the series (4.19) is smaller than or equal to the distance between x_s and the nearest singular point $\bar{x}$. Therefore, the series expansion (4.19) converges to the eigenvalues problem (4.11) solution at least at each station $x \in]-Fr/2, -Fr/2 + Fr/We^2[$.

Note that the physical domain extends from 0 to 1; therefore, we can conclude that for $-Fr/2 + Fr/We^2 > 1$ and, so, for

$$We < \sqrt{\frac{2}{2/Fr + 1}} \tag{4.20}$$

the series (4.19) represents, in principle, the complete analytic solution to the singular eigenvalues problem (4.11). The series, therefore, is not uniformly convergent, which means that the analytic solution of limited application. On the other hand, the singular location $\bar{x} = -Fr/2$ is not physically interesting because it is located outside the sheet domain for each Fr and, therefore, it does not need any special treatment.

With reference to the expansion (4.19), the boundedness condition of $\mathrm{d}\hat{\ell}/\mathrm{d}x$ in x_s can be formulated as

$$\lim_{x \to x_s} (x - x_s)^{n-1-(2Fr\lambda_r/We)} < \infty \quad \forall n. \tag{4.21}$$

Of course the boundedness condition affects the part real of the derivative of any series term only, because the imaginary one

$$\cos\left(\frac{-2Fr\lambda_i}{We} \log|x - x_s|\right) + \mathrm{i} \sin\left(\frac{-2Fr\lambda_i}{We} \log|x - x_s|\right) \tag{4.22}$$

is oscillating and results in being unconditionally bounded for $x \to x_s$.

Equation (4.21) yields

$$\lambda_r < -\frac{We}{2Fr} \tag{4.23}$$

and therefore we can conclude that, in a critical regime, not only is the spectrum unconditionally stable for each We and Fr, but it is subjected to the constraint of the maximum achievable growth rate. In other words, the growth rate is bounded. As will be seen, the numerical results will confirm this prediction.

https://doi.org/10.1017/jfm.2017.241 Published online by Cambridge University Press

4.2. *Numerical simulation*

To corroborate the asymptotic modal analysis, numerical simulations of the governing equations system (2.33)–(2.34) have also been carried out, by means of a standard finite-difference discretization. The initial condition is constituted by a compact support function satisfying the prescribed boundary conditions, namely a Gaussian-like pulse for the perturbed centreline of nappe, properly localized upstream or downstream of the singularity station depending on the flow regime nature, subcritical or supercritical, respectively. No perturbation in lateral velocity fluctuation v is considered here. Among the various possibilities analysed during the numerical tests, the most convenient numerical procedure appeared to be that based on the direct integration of the system of two equations (2.33)–(2.34). Bearing in mind the wave nature of the expected solution, we formally imposed just the reflecting condition, $\ell(0) = 0$, on (2.33), the free-outflow condition at the right boundary being self-guaranteed. It should be stressed that, as a consequence, at the inlet station the equation (2.33) is implicitly enforced as $v = U(\partial\ell/\partial x)$. No particular treatment has been added for the specific subcritical or supercritical regimes.

The numerical simulation of the spatio-temporal partial-derivative equations did not need any special trick for the presence of the singularity in subcritical regime. The large time simulation usually agrees perfectly with the corresponding eigenfunction from the modal analysis.

5. Results

Computed modes and oscillation frequencies of the liquid sheet occurring in the various flow regimes of *We* number will be presented in this section, with initial emphasis on the critical region, i.e. $We = O(1)$. In order to make calculations with physically relevant parameters, we first hypothesized to work with a water–air fluid couple ($\sigma = 0.073$ N m^{-1}, $\rho_l = 1000$ kg m^{-3}, $\gamma = 1.4$) at a base cavity pressure $P_a^\star = 10^5$ Pa (and standard ambient temperature), and we assumed also $Fr = O(1)$. Choosing the cavity height $L^\star = 0.15$ m (of the same order as the values reported by de Luca (1999) and by Finnicum *et al.* (1993), equal to 0.275 m and 0.305 m, respectively), and the slit width $H_{in}^\star = 0.1 \times 10^{-3}$ m (for instance, Finnicum *et al.* (1993) realized an inlet thickness of approximately 0.25×10^{-3} m), yields a sheet inlet velocity of $U_{in}^\star = 1.2$ m s^{-1} (as made by Binnie 1974; Sato *et al.* 2007; Mori *et al.* 2012). Thus, one can achieve both $Fr \simeq 1$ and $We \simeq 1$, with ε being equal to 0.67×10^{-3}. Finally, by taking into account that $W^\star/L^\star$ ranges typically from 0.2 (Schmid & Henningson 2002) to 1 (Binnie 1974), typical values of $\mathcal{K} = O(10^6)$ and $\mathcal{K} = O(10^5)$, respectively, are obtained. Furthermore, we will see also that for a typical geometrical configuration of Binnie (1974), the critical regime can be obtained also with a relatively low inlet velocity, thus having simultaneously $Fr = 0.077$ and $\mathcal{K} = 5 \times 10^5$.

Oscillation frequencies will be compared with experimental data from the literature which, are available in the supercritical regime at relatively high *We* numbers. In critical or subcritical regimes experimental results refer to geometrical configurations interacting on an unconfined ambient through both interfaces. Indeed, experimental findings are available in the critical regime for nominally axisymmetric liquid bells investigated by Brunet *et al.* (2004), who adopted inlet boundary conditions allowing modulations of the circumference on which the bell intersects the solid ceiling. These data are clearly not suitable for making comparisons with the behaviour of the flat configuration here analysed. In the model of Brunet *et al.* (2004) oscillations are

https://doi.org/10.1017/jfm.2017.241 Published online by Cambridge University Press

produced by surface tension-driven pressure variations (due to the bell deformation), whilst in the present sheet case oscillations are produced by isentropic pressure variations due to the displacement of the sheet centreline.

5.1. *Highlights of numerical simulations*

Systematic numerical simulations of spatio-temporal evolution of the interface deflection have been carried out, starting from an initial instant when a particular perturbation, a Gaussian-like bump, is imposed on the interface. No initial disturbance on the lateral velocity perturbation v has been considered. Due to the lack of experimental data in the subcritical regime, the numerical simulations have been utilized to validate the eigenvalues analysis, especially the treatment used to remove the singularity. A broad comparison with experimental results in the supercritical regime will be reported below. The temporal panels shown in figure 2 refer to the evolution computed for the subcritical case of $We = 0.82$ with $\mathcal{K} = 5 \times 10^4$, $\varepsilon = 6.7 \times 10^{-4}$, and to a bump disturbance initially located at $x = 0.1$, i.e. in the subcritical region $0 < x < x_s$, here resulting in $x_s = 0.24$ (4.9). Note also that other simulations, not shown herein, revealed that the asymptotic deflection eventually reached by the sheet is not influenced by the initial position of the disturbance. The panels reported in figure 2 show an initial bump splitting into two parts, one travelling rightwards and being rapidly expelled, the other one travelling leftwards, where both have the expected velocities. The reflection of the left part on the inlet boundary at $x = 0$ generates the temporary establishment of a low wavenumber mode which is rapidly characterized by the appearance of shorter wavelength ripples. At large times a travelling wave, exhibiting an almost regular structure with a wavenumber of approximately $k = 15$, is eventually established. Details about the transition from an initial impulse to the rise of capillary waves are presented in the movie, provided as supplementary material available at https://doi.org/10.1017/jfm.2017.241.

A comparison of large time sheet centreline deflection and lateral velocity between eigenmodes (*a*) and numerical simulations (*b*) is reported in figure 3, referring to the same parameters as the panels of the previous figure. The physical relevance of the result will be addressed later on, when discussing the shape of modes observed in actual experimental rigs.

The above comparisons appear quite satisfactory. In particular, note the perfect agreement of the two solutions near the singularity station $x_s = 0.24$, showing that the treatment of the singularity worked successfully in the spectral analysis. A further finding is the confirmation of the travelling wave feature of the solution; as was verified in a wide range of flow conditions, the wave velocity satisfies the following relationship to within good accuracy

$$\bar{a} = \frac{\lambda_i}{2\pi k}, \tag{5.1}$$

with λ_i indicating the disturbance circular frequency (i.e. the imaginary coefficient of eigenvalue) and k the wavenumber, which can be evaluated by inspecting the eigenfunctions. The average $\bar{a}$ velocity is, on the other hand, directly evaluated as $\bar{a} = 1/t_{cross}$, where the crossing time is

$$t_{cross} = \int_0^1 \frac{\mathrm{d}x}{U \pm \sqrt{\dfrac{U}{We}}}. \tag{5.2}$$

https://doi.org/10.1017/jfm.2017.241 Published online by Cambridge University Press

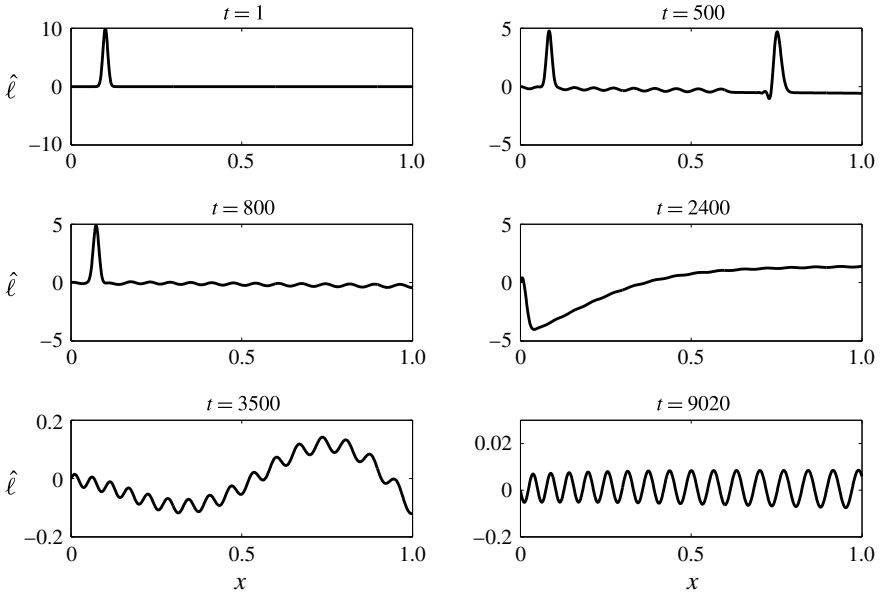


FIGURE 2. Temporal sequence of panels of instantaneous nappe deflection extracted from the numerical simulation of (2.33)–(2.34), for $We = 0.82$, $Fr = 1$, $\mathcal{K} = 5 \times 10^4$ and $\varepsilon = 6.7 \times 10^{-4}$.

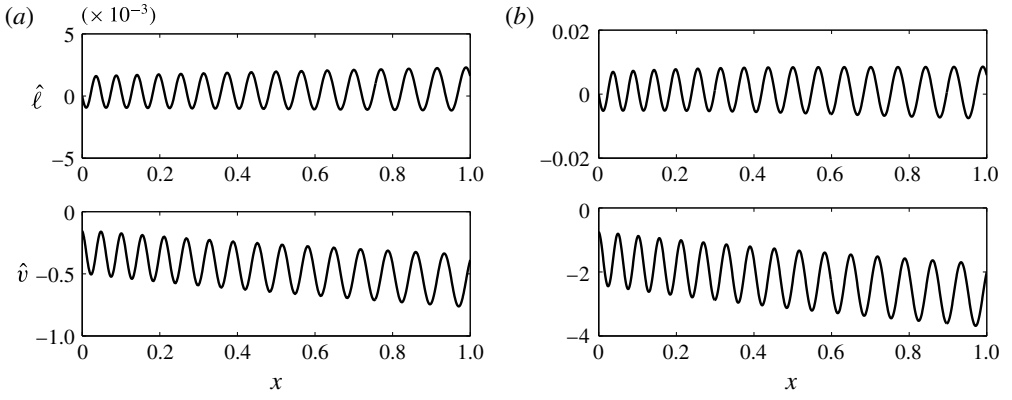


FIGURE 3. Comparison between leading eigenmode (*a*) and numerical simulation (*b*) of (2.33)–(2.34), for $We = 0.82$, $Fr = 1$, $\mathcal{K} = 5 \times 10^4$ and $\varepsilon = 6.7 \times 10^{-4}$.

5.2. *Analysis of critical regime*

Some significant results of the spectral analysis for *We* around unity will be hereafter presented. Figure 4 compares spectra obtained in subcritical ($We = 0.98$) and supercritical ($We = 1.02$) regimes for $Fr = 1$ and two typical values of the air stiffness, $\mathcal{K} = 10^5$ and $\mathcal{K} = 10^6$. As predicted before, the subcritical regime (for $We = 0.98$ it is $x_s = 0.021$) is characterized by one branch only (associated with the faster travelling wave with velocity $U + \sqrt{U/We}$), constituted by two symmetrical parts exhibiting outer cusp-point maxima, as well as local maxima (independent of $\mathcal{K}$) represented by the inner pair of eigenvalues. The configurations reported in figure 4(*a*) are stable.

https://doi.org/10.1017/jfm.2017.241 Published online by Cambridge University Press

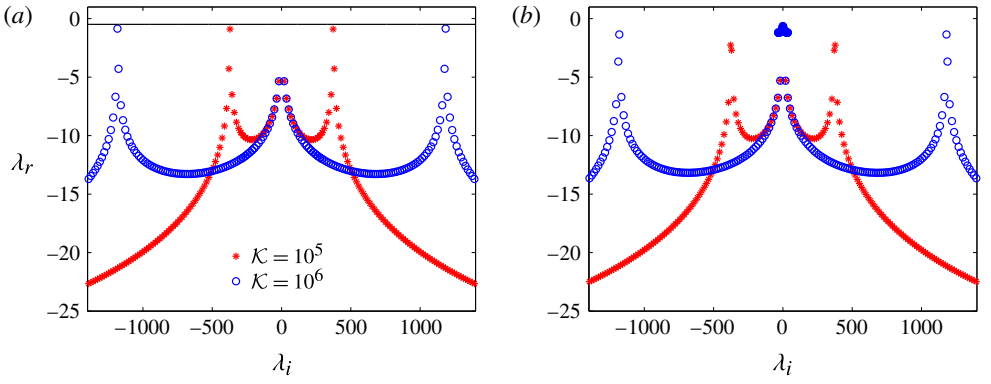


FIGURE 4. (Colour online) Spectra for $Fr = 1$, $\varepsilon = 6.7 \times 10^{-4}$ and selected $\mathcal{K}$ values. (*a*) $We = 0.98$, (*b*) $We = 1.02$.

Note also that, as already extensively discussed by De Rosa *et al.* (2014), according to the damped spring–mass model driven by the self-induced forcing f_i of (3.6), the frequency of the less stable eigenvalue approximately scales with $\sqrt{\mathcal{K}}$ (of course in the driven regime it coincides with that of the forcing term). Another characteristic frequency is represented by the constant spacing $\Delta\lambda_i$ of the imaginary parts of the eigenvalues which is related to the crossing time by $\Delta\lambda_i \approx 2\pi/t_{cross}$. The horizontal continuous line of figure 4(*a*) is the theoretical upper bound of inequality (4.23), which in the present case yields $\lambda_r < -0.49$ and therefore it is satisfied. Figure 4(*b*) reports spectra for $We = 1.02$ and the same values of $\mathcal{K}$ as the previous figure 4(*a*). Thus, the analysis of these two spectra sheds light on the critical region. The major feature is that, on the one the presence of a part of a branch representing the parametric continuation of the analogous branch found for $We = 0.98$ is noted, on the other a new nucleus of eigenvalues having growth rate weakly less than zero clearly arises. The new nucleus of eigenvalues is to be ascribed to the travelling waves with velocity $U - \sqrt{U/We}$ and to their interference with low-frequency eigenvalues associated with the faster waves with velocity $U + \sqrt{U/We}$. This last finding can be better appreciated by looking at figure 5(*a*,*b*), depicting the close-up views of the previous figures 4(*a*) and 4(*b*), respectively. It is very important to point out that in the above pictures the frequency scale is extended up to 1500 for the sake of completeness only, but values greater than approximately 300 are suspected not to have physical relevance because they are associated with high wavenumber modes, which are definitely damped by viscosity, while they also invalidate the assumption of thin sheet model. This issue will be raised again when discussing the comparison with experimental data in the supercritical regime. De Rosa *et al.* (2014) did not report this argument because their study was limited to a parametric investigation without further insights on the physical relevance of the higher-frequency modes.

A first estimate of the viscous dissipation in short wavelength capillary ripples can be made by following the approach of Lighthill (1978), in particular with reference to the so-called internal dissipation mechanism, i.e. under the assumption that the viscous damping is limited to the wave amplitude, with the main flow field being irrotational. This approach, well established more recently by Joseph, Funada & Wang (2007), is the basis also of the work of Longuet-Higgins (1997) dealing with capillary–gravity waves. Lighthill (1978) showed that the time constant $\tau^\star$ for the exponential decay of

https://doi.org/10.1017/jfm.2017.241 Published online by Cambridge University Press

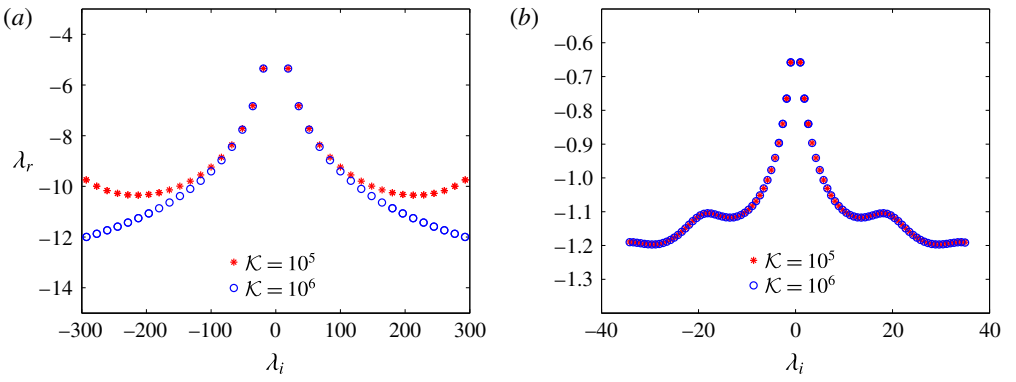


FIGURE 5. (Colour online) Inner eigenvalues of spectra for $Fr = 1$, $\varepsilon = 6.7 \times 10^{-4}$ and selected $\mathcal{K}$ values. (*a*) $We = 0.98$, (*b*) $We = 1.02$.

surface waves of wavelength $\lambda^\star$ is

$$\tau^\star = \frac{\lambda^{\star 2}}{16\pi^2 \nu}, \tag{5.3}$$

with ν being the fluid kinematic viscosity.

As asserted by Joseph *et al.* (2007), the wave attenuation can be evaluated by the distance (namely, the number of wavelengths) a wave travels before it decays by a certain amount, or, in other terms, by the number of oscillation periods, $T^\star$, corresponding to a given decay amount. Thus, the quantity $\tau^\star/T^\star$ measures the number of periods for the energy of sinusoidal waves to be reduced by a factor e. By assuming a constant sheet thickness, $T^\star$ is given by

$$T^\star = \lambda^\star \sqrt{\frac{\rho_l H^\star_{in}}{2\sigma}} \tag{5.4}$$

and the following is finally obtained

$$\tau^\star/T^\star = \frac{1}{16\pi^2} \frac{1}{Oh} \frac{\lambda^\star}{H^\star_{in}}, \tag{5.5}$$

where the Ohnesorge number is introduced as

$$Oh = \nu \sqrt{\rho_l/(2\sigma H^\star_{in})}. \tag{5.6}$$

For standard values of the thermodynamic properties of water, $H^\star_{in} = 10^{-3}$ m and $\lambda^\star/H^\star_{in} = 10$, one obtains $Oh = 2.62 \times 10^{-3}$ and $\tau^\star/T^\star \simeq 24$, while in the case of very short capillary ripples with $\lambda^\star/H^\star_{in} = 2$ the wave energy is expected to be reduced by a factor of e in approximately five periods. This last prediction is consistent with the experimental findings of de Luca & Costa (1997*b*) who visualized sinuous waves produced by an obstacle on a free-falling sheet. It is also important to note that, in the presence of surfactant agents in the liquid, another attenuation effect has to be taken into account, i.e. the surface dissipation, that can exceed the internal dissipation, as discussed by Lighthill (1978) and experimentally approached by de Luca & Costa (1997*b*), who took advantage of a previous work of de Luca & Meola (1995).

https://doi.org/10.1017/jfm.2017.241 Published online by Cambridge University Press

Figure 5(*a*) shows a detail of the lowest frequency eigenvalues (inner conjugate couples) calculated for $We = 0.98$ (but not less stable eigenvalues for $\mathcal{K} = 10^5$ and $\mathcal{K} = 10^6$), whilst figure 5(*b*) refers to the less stable supercritical ($We = 1.02$) eigenvalues (which are practically independent of $\mathcal{K}$) and it shows in great detail the interference of modes. Although for $We = 0.98$ the less stable modes are the higher-frequency ones scaling with $\sqrt{\mathcal{K}}$, the physical considerations above lead us to think that the sheet shapes more likely observable in experiments are represented by the inner modes (i.e. local maxima); the same should occur in the supercritical condition of $We = 1.02$, where the inner modes are the less unstable, too. The difference lies in the fact that in the subcritical regime, the prevailing modes are of fast type, whilst in the supercritical regime they are of slow type. In fact, in the former case the order of magnitude of the other characteristic frequency of the system, $\Delta\lambda_i \simeq 16.1$, is associated with the crossing time of the fast mode, whilst in the latter one $\Delta\lambda_i \simeq 0.75$ corresponds to the crossing time of the slow mode. The supercritical spectrum of figure 5(*b*) exhibits a wavy trend whose period is just $\Delta\lambda_i \simeq 16.1$, which evidences the interference between the modes. Finally, it is found that for $We = 0.98$ the ratio of the frequency local peak to $\Delta\lambda_i$ is approximately 1.18 and for $We = 1.02$ this ratio is approximately 1.27. This occurrence is reminiscent of the integer-plus-one-quarter resonance criterion of forced transverse vibrations of the nappe string, already uncovered by De Rosa *et al.* (2014) in the absence of surface tension. This will be discussed in more detail later on, in connection with comparisons with experimental data available in the literature for the supercritical regime and can also be verified by inspecting the relevant eigenmodes.

The inner leading modes are presented in figure 6 for $\mathcal{K} = 10^5$ and $Fr = 1$. Panels (*a*,*b*) refer to subcritical ($We = 0.98$) and supercritical ($We = 1.02$) regimes, respectively. Their comparison gives a picture of the sheet shape variation encountered when traversing the critical regime. The nappe oscillation frequency accordingly changes from 19.13 for the subcritical regime to 0.99 for the supercritical regime. This finding has to be validated through experimental investigations because of the absence of experimental data as regards the critical regime, and will be further discussed in the subsequent section.

5.3. *Insight into the supercritical regime*

A rather detailed comparison of the present theoretical predictions with experiments undertaken by Binnie (1974) and by Sato *et al.* (2007) in the supercritical regime will be made in this section. Such a comparison will also represent the validation of the interpretation of the results found in the critical regime. The apparatus arrangement of Binnie (1974) was very similar to that sketched in figure 1, concerning the formation of a thin sheet of water falling in air, in the presence of an air enclosure behind the sheet. Tests were carried out for various geometrical quantities and water flow rate values, so as to vary the Weber number (basically by increasing the water flow rate) in the range from 3.77 to 287 (the corresponding Froude number ranged from 0.28 to 7.69) and the dimensionless air stiffness $\mathcal{K}$ in the range from 10^5 to 10^3, respectively. Sheet oscillation frequency was measured by means a stroboscope and the associated deformed centreline shape was detected indirectly by means of an optical method able to individuate positions half a wavelength apart on the shape. Binnie (1974) predicted the modes associated with the natural frequencies of the nappe through a simplified physical model which did not include surface tension effects, and reported such modes for various testing conditions. With reference to his flow configuration, named A, with $We = 95.9$ and $\mathcal{K} = 5.87 \times 10^3$, panels (*a–d*) of

https://doi.org/10.1017/jfm.2017.241 Published online by Cambridge University Press

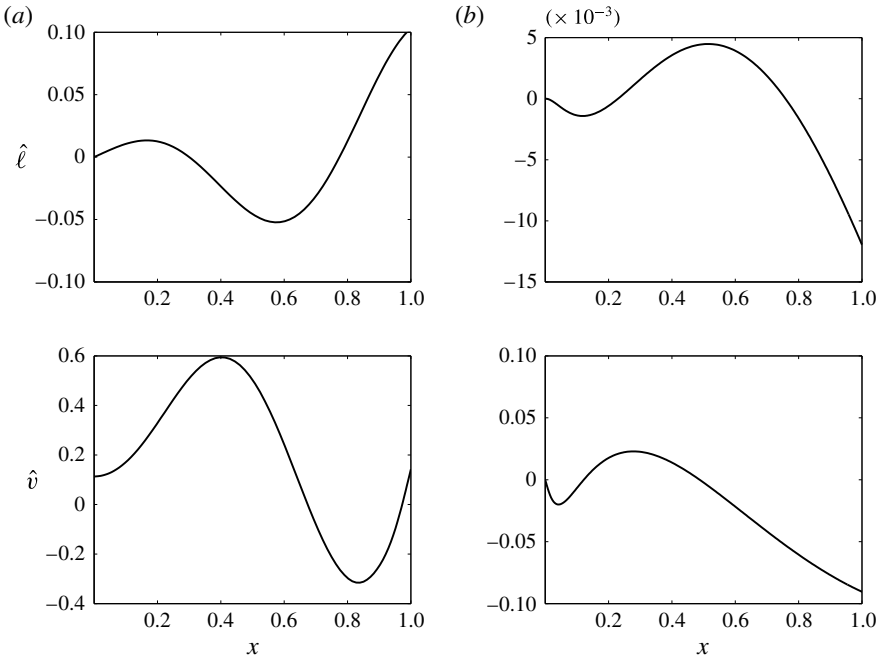


FIGURE 6. Inner leading eigenfunctions for $Fr = 1$, $\mathcal{K} = 10^5$ and $\varepsilon = 6.7 \times 10^{-4}$. (*a*) $We = 0.98$, (*b*) $We = 1.02$.

figure 7 show the first, second, third and fifth mode, respectively, corresponding to less stable inner eigenvalues, as discussed before in regard to the critical regime. Such modes agree strictly with the predictions arising from Binnie's theory which, in turn, agrees with his own experiments. Note that the peak frequency of the most unstable mode, namely the spring–mass frequency scaling with $\sqrt{\mathcal{K}}$, equal to approximately 80 (namely 154 Hz), was not observed in the experiment; on the contrary, the fifth inner mode was detected in this configuration.

A comparison between frequencies observed experimentally by Binnie (1974) and calculated by the present physical model is shown in table 1. The tests from A to D refer to the same geometrical configuration, while in test F a wider nozzle width was used to work with a higher liquid velocity. Table 1 shows a quite good agreement between frequencies observed in experiments, f_e^*, measured in Hertz, and frequencies evaluated numerically, f_n^*, by the present analysis. Note that Binnie (1974) too made a comparison between measured and calculated (via his simplified model) frequencies, f_b^*, and attributed the discrepancy of the data to the difficulty in measuring correctly the liquid inlet velocity. In any case, the present comparison is better than Binnie's. From Binnie's experiments it is evident that the nappe always oscillates at lower frequencies corresponding to inner modes (which are all stable) of the spectrum, because higher-frequency modes are most likely damped by viscosity. The order of the observed mode cannot be predicted, of course, by the present theory and no explanation in this respect was furnished by the author of the experiments.

Another systematic comparison has been made with reference to experimental tests of Sato *et al.* (2007), who carried out nappe shape visualizations and oscillation frequency measurements on an apparatus similar to that used by Binnie (1974).

https://doi.org/10.1017/jfm.2017.241 Published online by Cambridge University Press

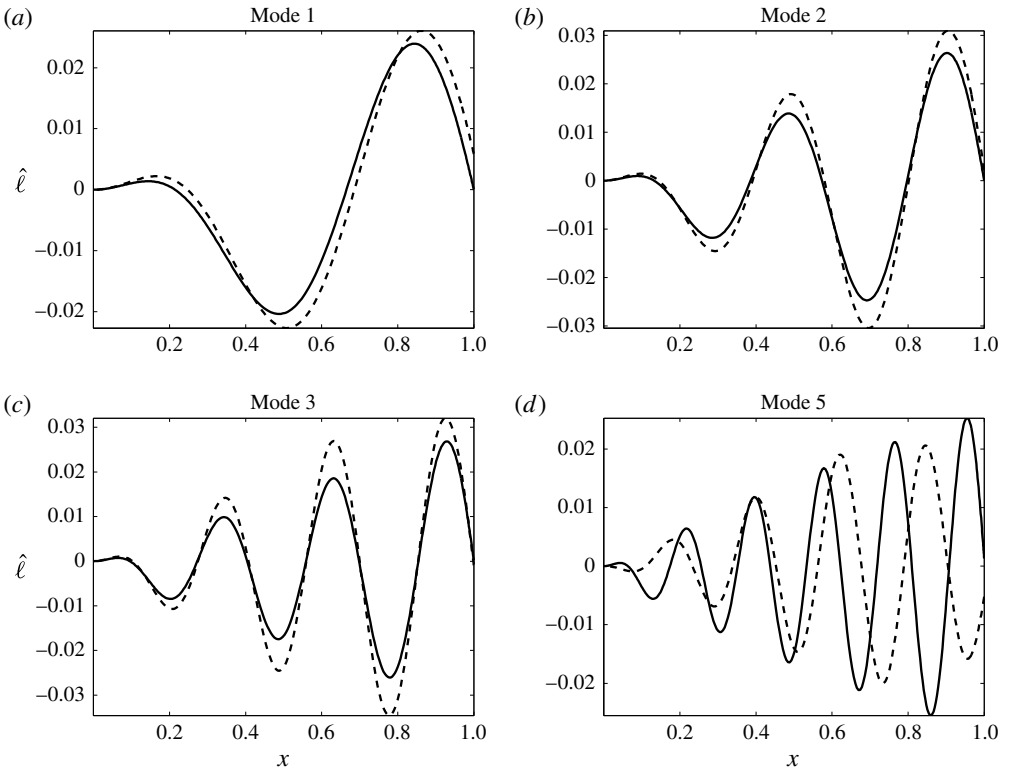


FIGURE 7. First, second, third and fifth eigenmodes for test A of Binnie (1974) ($We = 95.9$, $Fr = 7.69$, $\mathcal{K} = 5.87 \times 10^3$, $\varepsilon = 7.6 \times 10^{-4}$); the continuous lines refer to the present model, while the dashed lines refer to the Binnie's model not including the surface tension.

Test	We	$\mathcal{K}$	Fr	ε	f_e^* (Hz)	f_n^* (Hz)	f_b^* (Hz)	Mode
A	95.9	5.87×10^3	7.69	7.6×10^{-4}	60.5	65.48	70.44	5
B	39.24	9.9×10^3	3.57	9×10^{-4}	24.76	32.8	35.69	3
C	21.37	1.82×10^4	1.96	9×10^{-4}	13.11, 18.55	18.63, 23.3	20.1, 28.38	2, 3
D	3.77	1.63×10^5	0.28	7.3×10^{-4}	3.15	4.66	6.41	1
F	287.4	1.74×10^3	5.88	3.3×10^{-3}	22.9	28.76	28.8	2

TABLE 1. Comparison with experiments of Binnie (1974); f_e^* is the observed frequency, f_n^* is the frequency predicted by the present analysis, f_b^* is the frequency computed using Binnie's model.

However, Sato *et al.* (2007) made direct visualizations by using a high-speed camera and compared observed frequencies with pressure fluctuations in the closed chamber behind the nappe. Table 2 refers to data points corresponding to the smallest slit width considered by the above authors. For this series of tests the agreement between measured frequencies f_e^* and estimated frequencies f_n^* is satisfactorily strict. Again one should note that the (stable) modes selected by the flow system do not correspond to frequencies of the order of $\sqrt{\mathcal{K}}$, but to much lower values which are predicted by the inner eigenvalues. This point was outlined by Sato *et al.* (2007) who, furthermore,

https://doi.org/10.1017/jfm.2017.241 Published online by Cambridge University Press

We	$\mathcal{K}$	*Fr*	ε	f_e^* (Hz)	f_n^* (Hz)	f_b^* (Hz)	Mode
9.12	2.47×10^5	0.22	2.8×10^{-3}	5.26, 9.76	6.28, 9.06	6.49, 11.07	1, 2
12.16	1.85×10^5	0.29	2.8×10^{-3}	5.8, 10.54	6.65, 10.19	6.80,11.63	1, 2
15.2	1.48×10^5	0.37	2.8×10^{-3}	11.1	11.15	12.1	2
9.12	4.3×10^5	0.17	2.1×10^{-3}	8.1, 11.41	7.77, 10.54	9.26, 13.04	2, 3
12.16	3.22×10^5	0.22	2.1×10^{-3}	8.56, 12	8.68, 11.16	9.66, 13.61	2, 3
15.2	2.58×10^5	0.28	2.1×10^{-3}	9.14, 13.26, 17.45	9.34, 11.71, 15.58	10, 14.1, 18.17	2, 3, 4

TABLE 2. Comparison with experiments of Sato *et al.* (2007); f_e^* is the observed frequency, f_n^* is the frequency predicted by the present analysis, f_b^* is the frequency computed using Binnie's model.

pointed out that 'the generated frequencies remain the same even when the chamber width (i.e. W^*) was considerably changed'; in other words, they noted experimentally that the inner modes are independent of $\mathcal{K}$, as confirmed by the present theoretical analysis.

Both Binnie (1974) and Sato *et al.* (2007) measurements gave evidence of the integer-plus-one-quarter resonance criterion, which is fulfilled by the present analysis. In the experimental investigation reported by Schmid & Henningson (2002), on the contrary, the nappe is seen to oscillate at the frequency corresponding to the base flow falling time, although from their theoretical analysis it is evident that the lowest frequency is approximately 1.28 times of that corresponding to the falling time.

It seems very interesting to compare spectra computed for a relatively high supercritical Weber number, at which the effects of the surface tension begin to be negligible, and for the critical values of $We = 1.02$ and $We = 0.98$, hence just above and below the critical threshold, as illustrated in figure 8. The geometrical configuration of test A of Binnie (1974) is assumed as the starting condition, for which $We = 95.9$, $\mathcal{K} = 5.87 \times 10^3$, $Fr = 7.69$. Thus, due to the lack of experimental data in the subcritical regime, a virtual numerical experiment has been carried out by starting from the condition of test A of Binnie (1974) and reducing the liquid flow rate (i.e. velocity) until obtaining $We = 0.98$, $\mathcal{K} = 5.75 \times 10^5$, $Fr = 0.076$. Figure 8 uncovers the characteristic wavy trend of a supercritical regime and shows increasingly stable eigenvalues as the Weber number is reduced. Reducing the liquid flow rate from the value of test A of Binnie (1974) down to the value of the subcritical regime leads to the frequency variations reported in table 3 for the first five inner modes. For each mode, the frequency is at first reduced until the critical threshold is reached, then it sharply increases below $We = 1$, due to the emergence of fast modes in the subcritical regime. Figures 9 and 10 report first, second, third, fifth modes associated with the corresponding inner eigenvalues for $We = 0.98$ and $We = 1.02$, respectively, to be compared with the modes of figure 7 referring to $We = 95.9$.

With reference to the first mode only, figure 11 illustrates graphically the sharp increase in the frequency of mode 1 when entering the subcritical regime as the Weber number is reduced. The arrow indicates the frequency route and $\Delta\lambda_{i+}$ and $\Delta\lambda_{i-}$ represent the frequencies related to the crossing time of the fast and slow waves, respectively, which are analytically evaluated as

$$t_{cross\pm} = 2Fr \left[\frac{1}{2}\left(U|_1 - 1\right) \mp \frac{1}{\sqrt{We}}\left(\sqrt{U|_1} - 1\right) + \frac{1}{We} \log \frac{\sqrt{U|_1} \pm \dfrac{1}{\sqrt{We}}}{1 \pm \dfrac{1}{\sqrt{We}}} \right]. \tag{5.7}$$

https://doi.org/10.1017/jfm.2017.241 Published online by Cambridge University Press

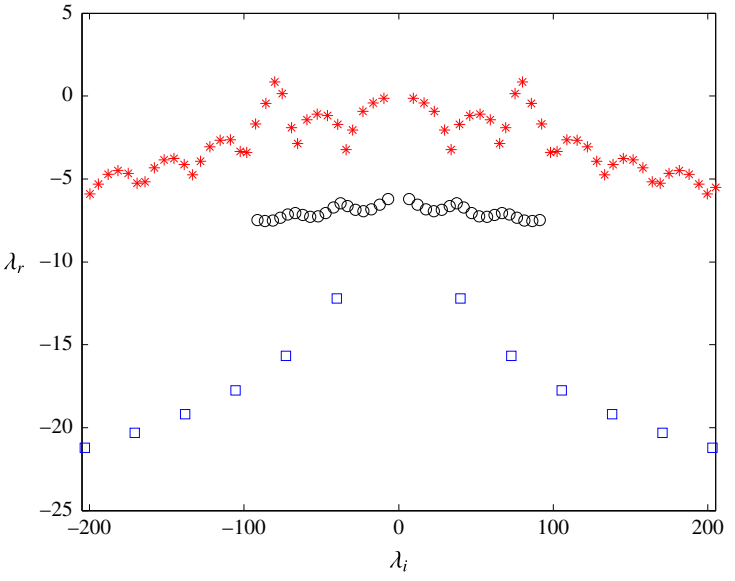


FIGURE 8. (Colour online) Spectra computed for various conditions of test A of Binnie (1974). $We = 95.9$, $\mathcal{K} = 5.87 \times 10^3$, $Fr = 7.69$ (∗); $We = 1.02$, $\mathcal{K} = 5.5 \times 10^5$, $Fr = 0.08$ (○); $We = 0.98$, $\mathcal{K} = 5.75 \times 10^5$, $Fr = 0.076$ (□).

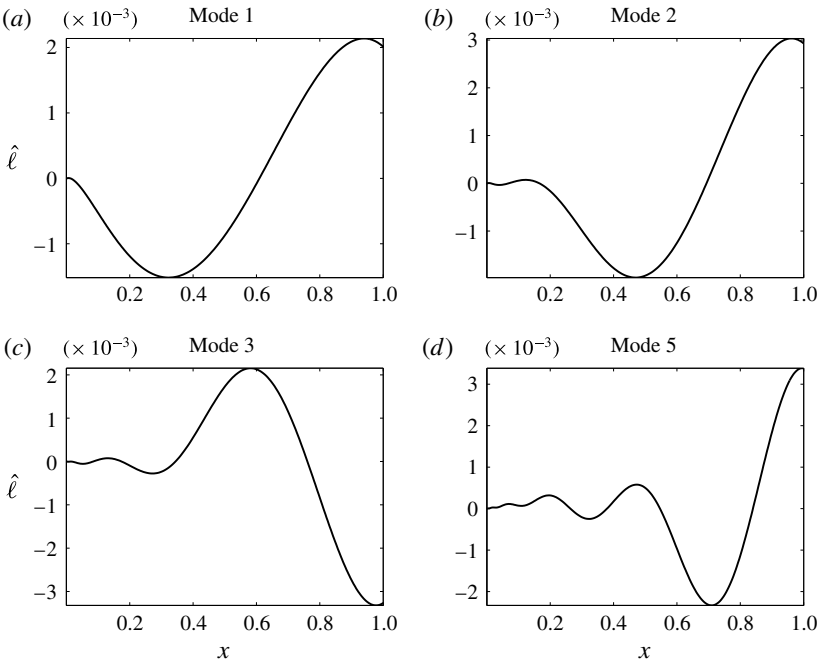


FIGURE 9. First, second, third and fifth eigenmodes for the test A of Binnie (1974) and for $We = 1.02$, $\mathcal{K} = 5.5 \times 10^5$, $Fr = 0.08$.

https://doi.org/10.1017/jfm.2017.241 Published online by Cambridge University Press

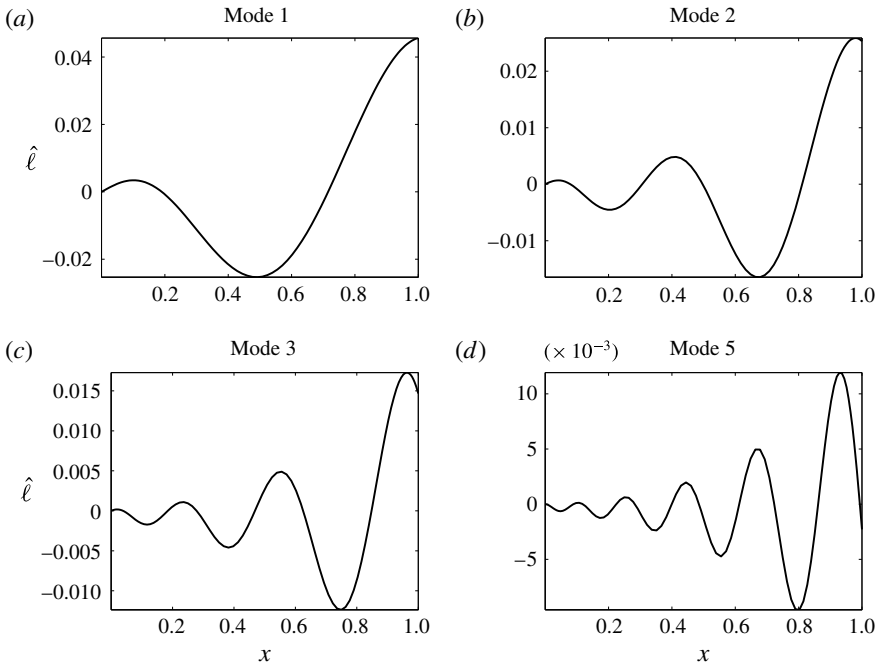


FIGURE 10. First, second, third and fifth eigenmodes for test A of Binnie (1974) and for $We = 0.98,\ \mathcal{K} = 5.75 \times 10^5,\ Fr = 0.076$.

We	$\mathcal{K}$	*Fr*	Mode 1 (Hz)	Mode 2 (Hz)	Mode 3 (Hz)	Mode 4 (Hz)	Mode 5 (Hz)
95.9	5.87×10^3	7.69	18.35	31.56	44.52	57.16	65.48
1.02	5.5×10^5	0.08	1.36	2.43	3.5	4.55	5.58
0.98	5.75×10^5	0.076	7.76	14.13	20.47	26.8	33.11

TABLE 3. Computed inner modal frequencies of test A of Binnie (1974) when reducing the liquid flow rate.

The result depicted in figure 11 requires an experimental validation. In addition, it should be used carefully because it refers to the inner first mode, and the present theory is not able to predict the actual selection mechanism of the frequency; hence, future experimental data should be compared with analogous routes referring to higher modes, and a jump from supercritical to subcritical modes of higher order cannot be excluded. Finally, to obtain the expected frequencies, one should multiply $\Delta\lambda_{i+}$ and $\Delta\lambda_{i-}$ by a factor equal to approximately 1.25 according to the one-plus-one-quarter resonance criterion.

Starting again from the condition of test A of Binnie (1974), and with reference to the first mode only, figure 12(*a*) depicts two routes towards the instability in the plane $Fr - \mathcal{K}$, the vertical one referring to an increase in the chamber width W^*, the hyperbolic one referring to an increase in the flow velocity U^*_{in}. In both cases the thick blue line corresponds to stable states, the dashed thick red line to unstable states. Because of the one-to-one correspondence between physical quantities

https://doi.org/10.1017/jfm.2017.241 Published online by Cambridge University Press

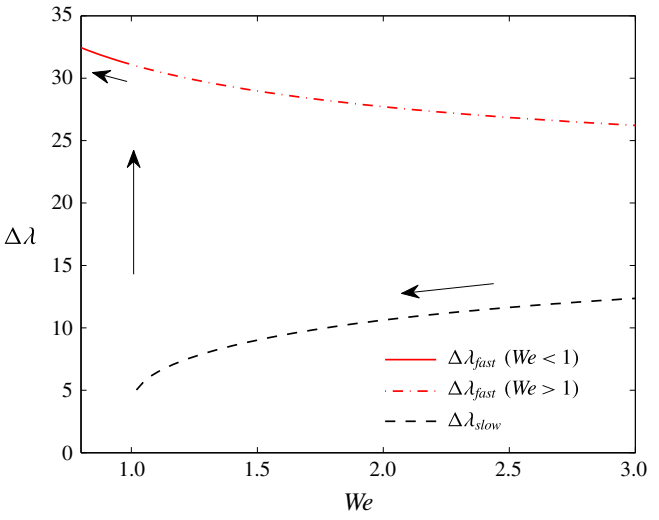


FIGURE 11. (Colour online) Frequency route from supercritical to subcritical regime; mode 1; $Fr = 0.077$.

and dimensionless parameters observed before for the case of water sheet flowing in air, the Weber number of each state is unique (for instance, in the starting point, denoted by the open circle symbol, it is $Fr = 7.69$, $\mathcal{K} = 5870$, $We = 95.9$) and the stable/unstable nature of a given status has to be inspected with reference to the neutral stability curve relative to that We value. In particular, along the vertical path the We number is constant, whilst along the other path We increases towards the instability. Such routes are depicted together with various neutral stability curves evaluated for We numbers equal to 95.9, 300.98, 10^4 (with this last value closely simulating the case of absence of surface tension). Note that $We = 95.9$ and $We = 300.98$ coincide with the stable–unstable marginal values along the two routes here considered. According to a previous finding of De Rosa *et al.* (2014), for each We number the unstable region is contained in between two marginal curves, with the lower ones being practically independent of the We number, as is better evinced in figure 12(*b*) illustrating the range of very low $\mathcal{K}$ values. The asymptotic value of $\mathcal{K} = 19.74$ attained for high Fr numbers uncovers the analogous result of De Rosa *et al.* (2014) who neglected the surface tension and defined the Froude number as the reciprocal of the present one. Figure 12(*a*) clearly shows the stabilizing role of the surface tension, because the unstable region is reduced with decreasing the Weber number. The subcritical regimes are always stable, as predicted by the Frobenius analysis. For the sake of completeness the inset of figure 12(*a*), corresponding to the dashed rectangle in the main panel, magnifies the range of Fr values less than 0.6 and gives an insight as regards the local minima of the upper marginal curves. Data reported in figure 12 have to be used very carefully because the system can exhibit higher modes in different flow conditions.

6. Conclusions

The dynamic behaviour of nappe oscillation has been revisited with reference to a physical model in which a thin liquid sheet interacts with a one-sided closed air

https://doi.org/10.1017/jfm.2017.241 Published online by Cambridge University Press

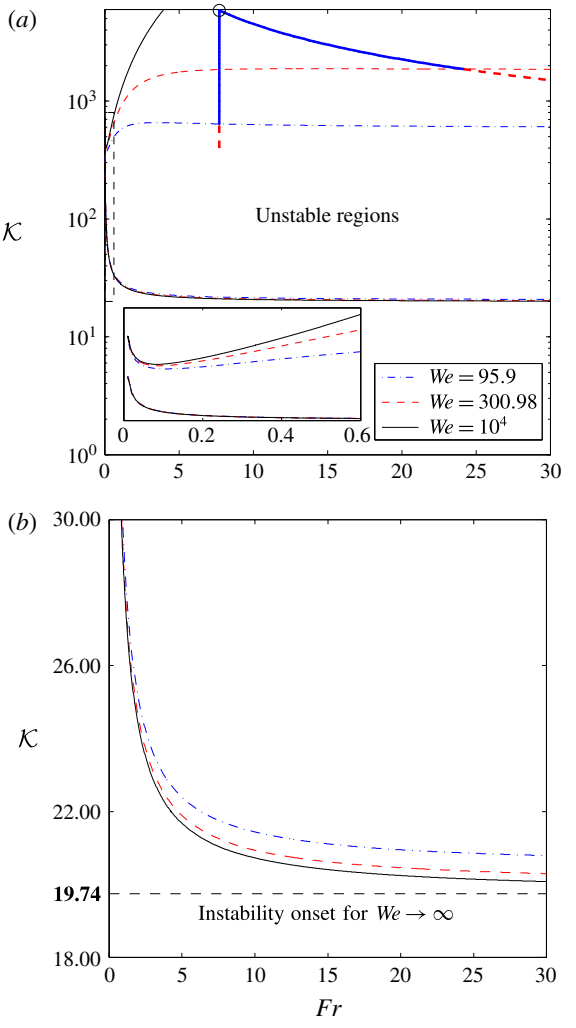


FIGURE 12. (Colour online) Curves of marginal stability and routes towards the instability. (*a*) The thick blue lines refer to stable states, the dashed thick red lines to unstable states; the inset represents the dashed rectangular range; the open circle is the condition of test A of Binnie (1974). (*b*) Trends for very low $\mathcal{K}$ values.

chamber. The mutual influence of the air within the enclosure with the compliant nappe interface self-induces a forcing whose features have been investigated. A major motivation for the work is given by the circumstance that, in the presence of surface tension effects, the equation governing the evolution of small disturbances exhibits a singularity at the vertical station where the local flow velocity equals the capillary waves velocity (critical station). The study has been carried out by developing a simplified inviscid, one-dimensional physical model in the context of a linearized formulation of free-interface convection dominated systems.

The modal analysis confirmed the physical argument that any disturbance evolves as the propagation of two wave fronts both directed downstream or one downstream and the other one upstream, depending on whether the flow is supercritical or subcritical,

https://doi.org/10.1017/jfm.2017.241 Published online by Cambridge University Press

respectively. In this respect the governing equation resembles that featuring the forced vibrations of a string of finite length, formulated in the reference frame moving with the flow velocity. From another perspective, the overall system behaves as a driven damped spring–mass oscillator, where the liquid sheet acts as the mass and the air enclosure as the spring. Thus, the dynamics of the flow system reveals two characteristic frequencies: that of the spring–mass behaviour scaling with the square root of the air chamber equivalent stiffness and that of the capillary waves travelling over the finite length sheet. In every situation the inlet section is considered as a perfectly reflecting boundary. As regards the other boundary condition, in the supercritical regime it is of null centreline slope at the inlet; in the subcritical regime it is imposed at just the singularity station by enforcing the boundedness requirement of the sheet slope there. The behaviour of the solution at the singularity point has also been investigated analytically by employing the Frobenius theory of singular ordinary differential equations.

The results of the modal analysis agree quite strictly with previous experimental data of the literature, available in the supercritical regime only, concerned with sheet deflection and oscillation frequency. A major point is that the spring–mass behaviour natural frequency was never detected in experiments, because high wavenumbers are damped by viscosity, although the related eigenmode is almost always the least stable one. Conversely, observed sheet shapes and measured frequencies are very much in agreement with lower-frequency modes and eigenvalues related to the propagation of waves over the forced vibrating sheet (inner local maxima of spectrum). It is worth noting that for the stable cases the dynamics of nappe oscillation turns out to be a frequency response problem, where the forcing frequency is a self-induced effect which is determined as a part of the solution.

As regards the critical regime of $We = O(1)$, where experimental data for the flat nappe configuration are missing, the major theoretical result is a sharp increase in the oscillation frequency as the flow Weber number is gradually reduced, from supercritical to subcritical values, due to the shift of the prevailing mode from the slow one to the fast one. This conclusion needs of course a careful experimental validation. Marginal stability curves and routes towards the instability are discussed as well.

Supplementary movie

Supplementary movie is available at https://doi.org/10.1017/jfm.2017.241.

REFERENCES

BARLOW, N. S., HELENBROOK, B. T. & LIN, S. P. 2011 Transience to instability in a liquid sheet. *J. Fluid Mech.* **666**, 358–390.

BENDER, C. M. & ORSZAG, S. A. 1999 *Advanced Mathematical Methods for Scientists and Engineers: Asymptotic Methods and Perturbation Theory*. Springer.

BINNIE, A. M. 1974 Resonating waterfalls. *Proc. R. Soc. Lond.* A **339**, 435–449.

BOYCE, W. E. & DIPRIMA, R. C. 2008 *Elementary Differential Equations and Boundary Value Problems*. Wiley.

BRUNET, P., CLANET, C. & LIMAT, L. 2004 Transonic liquid bells. *Phys. Fluids* **16**, 2668–2678.

COPPOLA, G., DE ROSA, F. & DE LUCA, L. 2013 Surface tension effects on the motion of a free-falling liquid sheet. *Phys. Fluids* **25** (6), 062103.

COPPOLA, G. & DE LUCA, L. 2006 On transient growth oscillations in linear models. *Phys. Fluids* **18** (7), 078104.

https://doi.org/10.1017/jfm.2017.241 Published online by Cambridge University Press

CROOKSTON, B. & TULLIS, B. 2013 Hydraulic design and analysis of labyrinth weirs. II: nappe aeration, instability, and vibration. *J. Irrig. Drain Engng* **139** (5), 371–377.

DE LUCA, L. 1999 Experimental investigation of the global instability of plane sheet flows. *J. Fluid Mech.* **399**, 355–376.

DE LUCA, L. & COSTA, M. 1997*a* Instability of a spatially developing liquid sheet. *J. Fluid Mech.* **331**, 127–144.

DE LUCA, L. & COSTA, M. 1997*b* Stationary waves on plane liquid sheets falling vertically. *Eur. J. Mech. (*B*/Fluids)* **16** (1), 75–88.

DE LUCA, L. & MEOLA, C. 1995 Surfactant effects on the dynamics of a thin liquid sheet. *J. Fluid Mech.* **300**, 71–85.

DE ROSA, F. 2013 Dinamiche instazionarie ed instabilita' lineare globale di getti liquidi. PhD thesis, Universita' di Napoli Federico II, http://www.fedoa.unina.it/9459/.

DE ROSA, F., GIRFOGLIO, M. & DE LUCA, L. 2014 Global dynamics analysis of nappe oscillation. *Phys. Fluids* **26** (12), 122109.

FINNICUM, D. S., WEINSTEIN, S. J. & RUSHAK, K. J. 1993 The effect of applied pressure on the shape of a two-dimensional liquid curtain falling under the influence of gravity. *J. Fluid Mech.* **255**, 647–665.

HOWISON, S. 2005 *Practical Applied Mathematics*. Cambridge University Press.

JOSEPH, D. D., FUNADA, T. & WANG, J. 2007 *Potential Flows of Viscous and Viscoelastic Fluids*. Cambridge University Press.

KINSLER, L. E., FREY, A. R., COPPENS, A. B. & SANDERS, J. V. 2000 *Fundamentals of Acoustics*. John Wiley & Sons.

LE GRAND, N., BRUNET, P., LEBON, L. & LIMAT, L. 2006 Propagating waves pattern in a falling liquid curtain. *Phys. Rev.* E **74**, 026305.

LIGHTHILL, J. 1978 *Waves in Fluids*. Cambridge University Press.

LIN, S. P., LIAN, Z. W. & CREIGHTON, B. J. 1990 Absolute and convective instability of a liquid sheet. *J. Fluid Mech.* **220**, 673–689.

LONGUET-HIGGINS, M. S. 1997 Viscous dissipation in steep capillary-gravity waves. *J. Fluid Mech.* **344**, 271–289.

MEHRING, C. & SIRIGNANO, W. A. 1999 Nonlinear capillary wave distortion and disintegration of thin planar liquid sheets. *J. Fluid Mech.* **388** (69), 69–113.

MORI, H., NAGAMINE, T., ITO, R. & SATO, Y. 2012 Mechanism of self-excited vibration of a falling water sheet. *Trans. Japan. Soc. Mech. Engrs* C **78** (792), 2720–2732.

NAUDASCHER, E. & ROCKWELL, D. 1994 *Flow-Induced Vibrations: An Engineering Guide*. Dover.

RAMOS, J. I. 2001 Singularities and stability of inviscid, planar liquid membranes. *Intl J. Engng Sci.* **39**, 1935–1948.

RAMOS, J. I. 2003 Oscillatory dynamics of inviscid planar liquid sheets. *Appl. Maths Comput.* **143**, 109–144.

SATO, Y., MIURA, S., NAGAMINE, T., MORII, S. & OHKUBO, S. 2007 Behavior of a falling water sheet. *J. Environ. Engng* **2**, 394–406.

SCHMID, P. J. & HENNINGSON, D. S. 2002 On the stability of a falling liquid curtain. *J. Fluid Mech.* **463**, 163–171.

SCHWARTZ, H. I. 1964 Nappe oscillation. *J. Hydraul. Div.* **90** (6), 129–143.

WEINSTEIN, S. J., CLARKE, A., MOON, A. G. & SIMISTER, E. A. 1997 Time-dependent equations governing the shape of a two-dimensional liquid curtain. Part 1. Theory. *Phys. Fluids* **9**, 3625–3636.

https://doi.org/10.1017/jfm.2017.241 Published online by Cambridge University Press